Title
OPTICAL COHERENCE TOMOGRAPHY AS AN ADVANCED TOOL IN DIFFERENT APPLICATIONS

Author
Yu, Junxiao

Publication Date
2019

Peer reviewed|Thesis/dissertation

UNIVERSITY OF CALIFORNIA,
IRVINE

OPTICAL COHERENCE TOMOGRAPHY (OCT) AS AN ADVANCED TOOL IN DIFFERENT APPLICATIONS

THESIS

submitted in partial satisfaction of the requirements
for the degree of

MASTER OF SCIENCE

in Biomedical Engineering

by

Junxiao Yu

Thesis Committee:
Professor Zhongping Chen, Chair
Professor William Tang
Professor James Brody

2019

TABLE OF CONTENTS

ACKNOWLEDGEMENTS

I would like to express the deepest appreciation to my committee chair, Professor Zhongping Chen, who has supported me and guided me through my whole master period. It is Dr. Chen who encourages me to keep moving forward when I come across difficulties. Without his persistent help, this dissertation would not have been possible.

I would like to thank my committee members, Professor William Tang and Professor James Brody, who were willing to spend their time helping me with the thesis and giving me suggestions.

In addition, a thank you to my lab members Jiang Zhu, Yan Li, Rachel Qu, Tiancheng Huo and Youming He at the Beckman Laser Institute. Jiang Zhu taught me a lot of optical coherence tomography knowledge and introduced lab systems to me. Yan Li, one of my best friends, supported and helped me throughout and shared her lab experience and knowledge with me without hesitation. Rachel, Tiancheng, and Youming also gave me a lot of suggestions during my research.

A very special thank you to my senior leader, Dr. Sucbei Moon, guided me through the polarization sensitive optical coherence tomography project step by step. Without him, the PS-OCT project would not be possible.

Also, I would like to thank my parents who provide me not only financial support but, more importantly, provide me with the moral support that has given me the opportunity to study at the University of California, Irvine, my dream school.

Finally, I'd like to thank all the people who have helped during my master years, Clare Chen, Xiangqun Xu, Emon Heidari, Linda Chandler, Jan Fisher, Tanya Burney.

ABSTRACT OF THE THESIS

Optical Coherence Tomography (OCT) as an Advanced Tool in Different Applications

By

Junxiao Yu

Master of Science in Biomedical Engineering

University of California, Irvine, 2019

Professor Zhongping Chen, Chair

Optical coherence tomography (OCT) is a non-invasive imaging technique that uses coherence light to acquire information from light scattering material. Based on its high-resolution, cross-sectional and three-dimensional volumetric image properties, it has become a major optical imaging modality in biomedical optics and medicine [1] . Optical coherence electrography (OCE) is an extension of OCT, it gives out optical elastic imaging based on tissue biomechanical properties which provides more information compared to traditional OCT [2, 3]. Another functional extension of OCT is known as polarization sensitive optical coherence tomography (PS-OCT). Different from intensity-based OCT, PS-OCT provides additional contrast information on tissues based on polarization states of light [4]. During my master period, I mainly focused on the applications of the OCT, including 1) OCT in early diagnosis on androgenic alopecia; 2) real-time viscosity-based monitoring of blood coagulation by OCE; 3) and PS-OCT with spun fiber.

Introduction

OCT is a non-invasive medical imaging technique that can provide intensity-based biological imaging with a high resolution in light scattering materials [5]. It uses near-infrared light as a source to detect tissues' biological properties and provide cross-sectional and volumetric imaging by measuring the magnitude and echo time of the backscattered light [1]. The use of a long central wavelength light make it possible to penetrate deeper in the scattering material. Based on the different biological properties of the material, the area that reflects more light shows higher signal, therefore, generating intensity-based the OCT images. This unique feature of OCT makes it a powerful imaging tool in many clinical applications.

In my study, I will focus on the applications of OCT, including 1) OCT in early diagnosis on androgenic alopecia; 2) real-time viscosity-based monitoring of blood coagulation by OCE and 3) PS-OCT with spun fiber.

Androgenic alopecia, more commonly known as pattern baldness, presents as a receding or thinning hairline in both men and women. OCT can rapidly provide near-histopathological cross-sectional images which can be used as a tool for in-vivo assessment of hair loss.

PS-OCT is a functional extension of OCT. It provides additional information of the sample based on analysis of polarization states of the backscattering light. Several PS-OCT systems, such as free-space optics, single mode fiber, and polarization maintaining (PM) fibers, have been developed. However, the traditional PM fiber preserves polarization states but has limitations

when implemented for a rotating endoscopic or catheter probe [6]. In this study, I developed a novel scheme of PS-OCT implementation using a specific PM fiber, known as a spun fiber, which has the structure of a PM fiber twisted along the fiber optic axis and distinguishes two circular polarization states with different propagation speeds. The spun fiber has the advantages of maintaining the polarization states regardless of fiber bends. The orientation insensitivity of the spun fiber offers great potential in the endoscopic PS-OCT system. I tested our spun fiber-based PS-OCT system on a chicken breast sample. The phase retardation image shows clear muscle structures compared to intensity-based OCT images, indicating our PS-OCT system has the ability to detect tissue birefringence.

A rapid and accurate clot diagnosis system is important in the assessment of blood coagulation. Traditional ways for blood coagulation assessment have poor sensitivity, poor repeatability, and lack of common standardization [7]. My lab member and I developed a piezoelectric transducer optical coherence elastography (PZT-OCE) system that enables real-time monitoring of blood coagulation based on the measurement of viscosity during the coagulation process. The system compared blood coagulation metrics between samples with different concentrations of activator kaolin and hemodilution. The results show that PZT-OCE is sensitive to coagulation abnormalities and able to characterize blood coagulation which can be used for diagnosis of coagulation disorders and monitoring of therapies.

Chapter 1

Early Diagnosis of Androgenic Alopecia with OCT

The American Hair Loss Association states that hair loss is an extremely emotionally distressing disease that makes afflicted patients psychologically vulnerable. Androgenic alopecia is more commonly known as pattern hair loss [8]. It presents as a receding hairline for men and hair thinning for women. Hair comes from hair follicles and undergoes cycles of growth (anagen), resorption (catagen), and rest (telogen). Follicular stem cells are responsible for the regeneration of the hair follicle with each new cycle. However, many factors may alter the regenerating hair follicle with subsequent interruption and hair loss (alopecia). It is believed that male pattern hair loss is mainly due to a combination of genetics and the male hormone dihydrotestosterone (DHT) [8]. The male hormone translates into DHT which block hair follicle regeneration by preventing hair follicle stem cells translating into hair follicle cells. Therefore, hair follicles become smaller and move away from the capillaries that provide nutrients to the hair, causing the hair to become thin and finally die.

The current gold standard of diagnosis includes non-invasive dermoscopy of the scalp, known as trichoscopy, and invasive punch biopsy. Trichoscopy, more like a microscope, magnifies the images of the surface of the scalp, which provides a very superficial understanding of hair diameter as well as the opening of the hair follicles. However, it can't assess information underneath the scalp and thus yields insufficient insight towards the cause of hair loss. Also, the diagnostic accuracy rate is only 50% to 70%, indicating the need for additional diagnostic tools.

Compared to trichoscopy, histopathological analysis provides more information, such as hair follicle density and hair shaft diameter, which can be used to infer the extent of androgenic alopecia development. Because of the invasive nature of punch biopsies, physicians cannot properly sample large areas of the scalp to avoid causing further pain to patients. Therefore, based on the current diagnostic techniques, it is difficult for physicians to get a global assessment of androgenic alopecia. OCT, as a non-invasive, non-ionizing tomographic imaging technique, can rapidly provide near histopathological cross-sectional image with a high resolution of 10 μm. Also, it can assess information on large areas of the scalp.

Platelet-rich plasma (PRP) is an autologous preparation of human plasma with a high concentration of platelets. It is prepared from centrifuging a subject's own blood with the subsequent extraction of the portion of plasma that is rich in platelets, growth factor, chemokines, and cytokines. Those growing factors can stimulate the hair follicle stem cells and therefore active the dominant hair follicles. In cooperate with people from the Department of Dermatology, we used a PRP treatment on a group of volunteer patients and imaged the same spot of the scalp before and after treatment.

A schematic diagram of the OCT system is shown in Figure 1. The OCT system used a swept source laser with a center wavelength of 1310 nm and frequency of 100 kHz. The beam was then split by a coupler with 90% of the power going into the sample arm while 10% went to the reference arm. It provided an 8 μm axial resolution and 16 μm lateral resolution with a 5 mm x 7 mm scanning window.

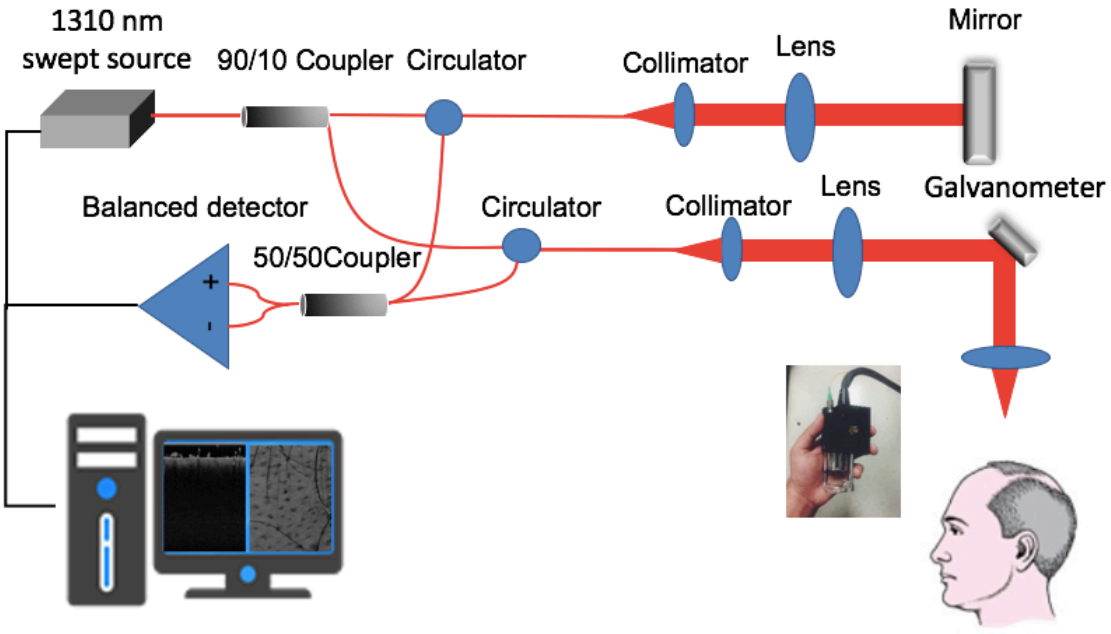

Figure 1. Schematic diagram of the OCT system. When scanning, the OCT probe was placed tightly on the patients scalp for a 3D scanning. For each spot, three groups of images were imaged.

For each patient, three fixed spots were measured: the frontal midline (FM), the central (CM) and the parietal midline (PM). Other spots were selected based on the conditions of the patients' affected areas.

To ensure the same scanning spot every time of the affected area, a unique handmade cap which had holes for the affected area for scanning was used for every patient. For each patient, we imaged the same spot before and 3 weeks after the treatment of PRP to see a comparison between the two.

Figure 2 shows photos of the affected area and the OCT images from left front (FL), central midline (CM), right front (FR) and crown before PRP treatment. The round shaped areas are the

hair follicles while the black lines indicate the hair shaft. Because light can't penetrate the hair, the black lines are shadows of the hair shafts.

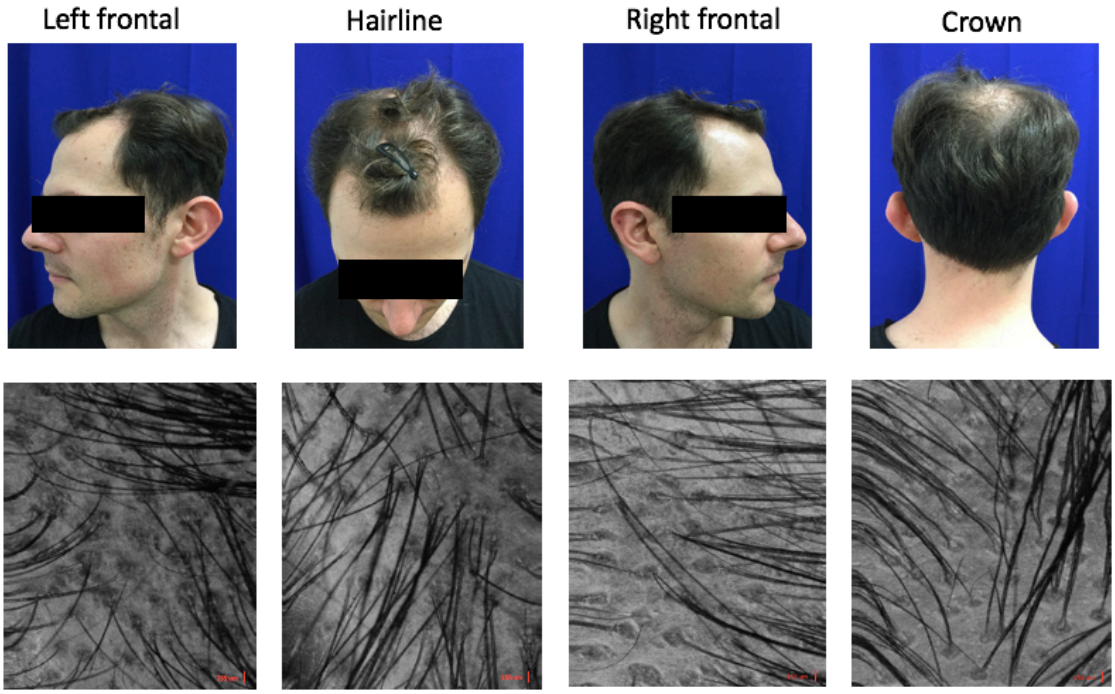

Figure 2. OCT images of the affected area from FL, CL, FR and crown. Shadowed round shaped areas are the opening of the hair follicles while the black lines indicated the hair shaft.

OCT images showed a clear view of the hair follicles that were underneath the scalp. Based on the OCT images, the density of the hair follicles and the diameter of hair follicles, as well as the diameter of hair shaft, can be measured and used as a persuasive parameter for the diagnosis for hair loss.

We also incorporated patients who underwent PRP treatment. The images are shown in Figure 3. The images were acquired before and after PRP treatment on the right frontal affected spot for both the patient 1 and patient 2. For both patients, there were a number of tiny hair follicles that were difficult to see before PRP treatment while they became bigger after three weeks of

treatment. Thin newly grown hair shafts were also observed in both post-treatment images, indicating the rebirth of hair follicles. The number of hair follicles and diameter of the hair follicles are shown in Figure 3 (B) and (D). Both the number and diameter significantly increased.

A Pre-treatment Post-treatment

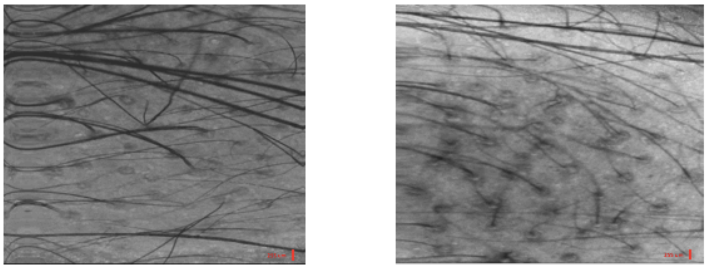

B

	Fol_num	Fol_dia/um
Pre	49	166.42
Pos	72	204.67

C Pre-treatment Post-treatment 3

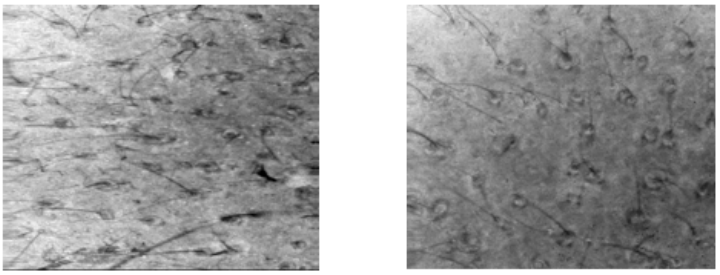

D

	Fol_num	Fol_dia/um
pos	60	173.06
pos2	64	206.88

Figure 3. OCT images of hair follicles underneath scalp before and three weeks after PRP treatment. A), B) OCT images and hair follicle number and diameter of the same spot before and after three weeks for patient 1; C), D) OCT images and hair follicle number and diameter of the same spot before and after three weeks for patient 2.

Therefore, our OCT system has successfully shown the ability to characterize hair follicles as well as to evaluate the diameter of the hair follicle and shaft. Also, it can observe the difference between the pre-treatment and post-treatment patient.

Chapter 2

Optical Coherence Elastography

OCE is an extension of OCT. It detects sample deformation, sample vibration, or shear wave propagation which has been developed to assess tissue biomechanics [9, 10]. Changes in mechanical properties of biological tissues can be used as a tool for early diagnosis of clinical diseases [11]. However, elasticity measurements of soft tissues require high spatial resolution. Recently, OCE, based on Doppler OCT as the imaging technique, has been widely applied in the elasticity detection of ocular tissues, breast tissues, vascular tissues, blood samples, muscular tissues, skin tissues and other biological tissue [12]. OCE has a high resolution of ~15 μm. Based on the measurement of vibration amplitudes and elastic wave velocities, elastic properties such as Young's modulus can be quantified. Working with my lab mate, we used OCE as an advantageous tool to monitor viscosity during hemodiluted blood coagulation. Furthermore, in order to get elastic information along the force direction during the OCE excitation, we performed coaxial excitation longitudinal shear wave measurements for quantification of elastic moduli along the force direction using an M-scan on different stiffness phantoms.

2.1 Longitudinal Shear Wave Measurement

Conventional transverse elastic wave measurement only quantifies the elastic modulus perpendicular to the force while missing elastic information along the force direction. Different from the transverse wave, the longitudinal shear wave can detect the elastic modulus along the

force direction under orthogonal excitation, which provides more information during measurements. In this study, we used a ring-shaped PZT to generate a longitudinal shear wave on the sample and an OCT system to visualize the vibration and wave propagation. Both the PZT and OCT system were located on the top of the testing sample while the PZT was in slight contacting with the sample surface. During the measurement, the PZT applied a force on the sample, and the OCT laser beam passed through the ring hole of the PZT, providing a coaxial lateral scan for the measurement of elastic properties along the force direction. However, incorporating a non-coaxial lateral scan, the Rayleigh wave can be captured and help acquiring information perpendicular to the force direction. Therefore, the elastic properties can be quantified not only perpendicular to the force direction but also along the force direction. The OCE system schematic diagram is shown in Figure 4 a).

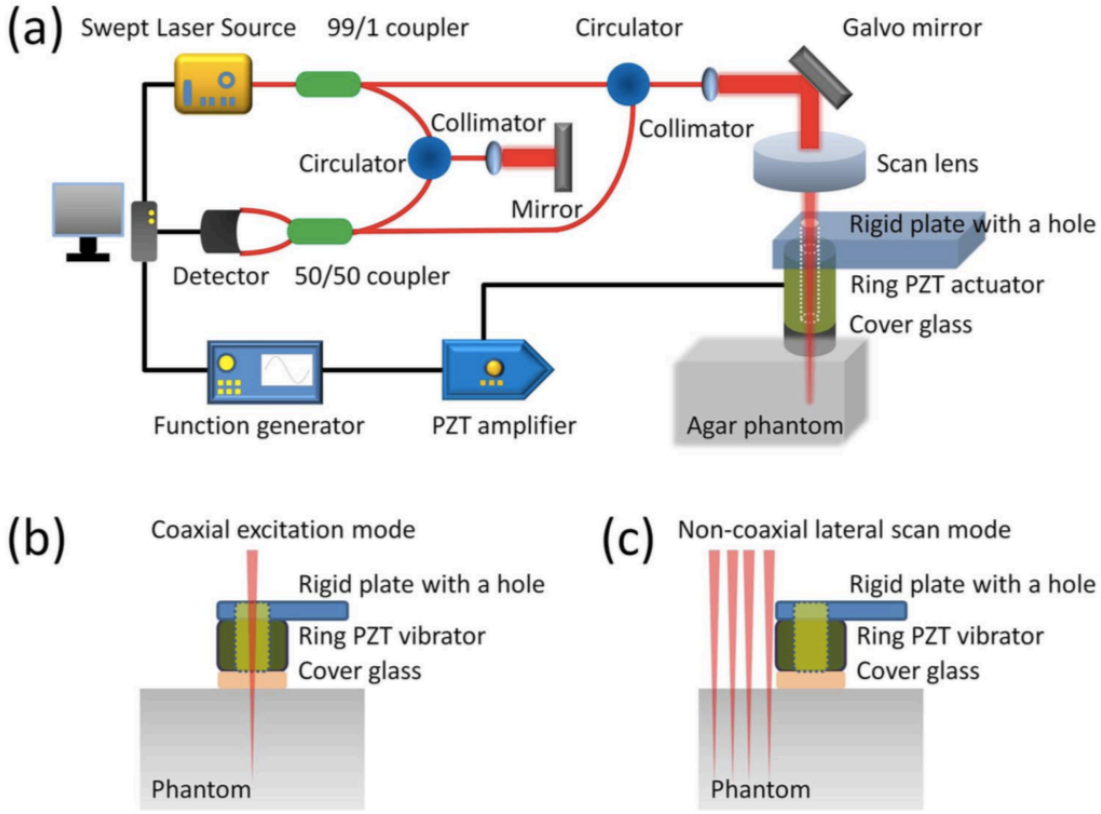

Figure 4. Schematic diagram of the OCE system for coaxial longitudinal shear wave measurements. a) The OCE system includes a swept source OCT unit and a ring PZT excitation unit. One end of the PZT is fixed on the rigid plate for stabilization and the other end is attached to a piece of cover glass to apply uniform force on the sample. b) The coaxial excitation mode. The OCT beam passes through the hole of the rigid plate, the ring actuator and the cover glass to provide a scan of the sample. c) Non-coaxial later scan mode. The OCT beam directly scanned the sample phantom [13].

An OCT imaging system and a PZT excitation unit were included in the OCE system. The OCT system used a swept source laser with a center wavelength of 1300 nm and frequency of 100 kHz. The beam was then split by a coupler with 99% of the power going into the sample arm while 1% went to the reference arm. The ring-shaped PZT had an inner diameter of 4.5 mm and an outer diameter of 8 mm. The PZT was fixed by a rigid plate for stabilization. A cover glass was gently placed on the surface of the phantom, and the other side was attached tightly to PZT to help

provide a uniform force on the sample. During scanning, the OCT beam which approximately coincided with the axis of the ring PZT actuator in the coaxial setup, shown in Figure 4 b), passed through the hole of the rigid plate, the ring PZT, and the cover glass. We imaged the phantom with 1000 A-lines within 10 ms while the PZT starting providing force at 1 ms. Also, the Rayleigh wave was measured using non-coaxial OCT lateral scans, shown in Figure 4 c), allowing the OCE system to acquire elastic information perpendicular to the force direction. For the experiment, PZT repeatedly excited the sample using one cycle of a sine wave with a frequency of 1 kHz and a peak-to-peak voltage of 103 V for each M-scan during OCT lateral scanning. Three waves were generated during the excitation, a Rayleigh wave, a compressional wave, and a shear wave, which are shown in Figure 5.

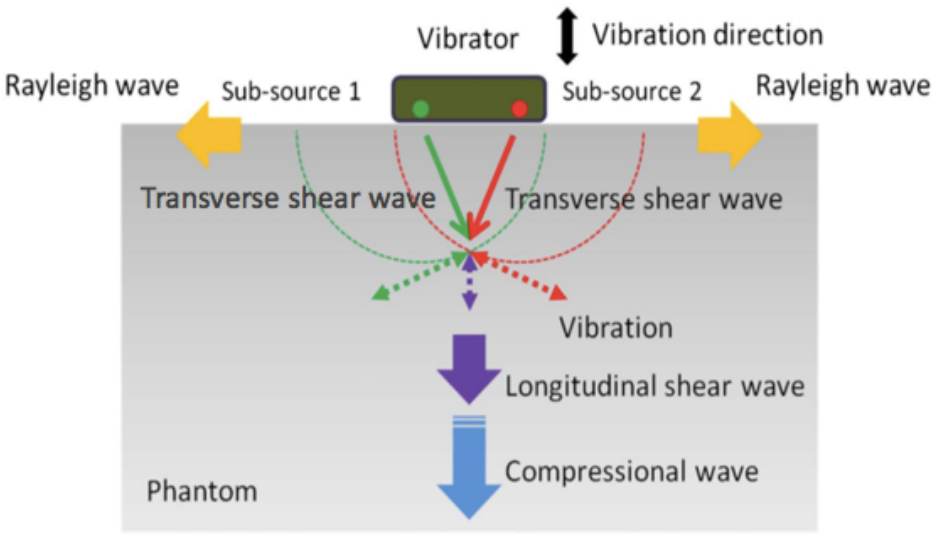

Figure 5. Generation of a transverse shear wave, a longitudinal shear wave and a compressional wave. The Rayleigh wave propagated near the surface of the sample. Multiple transverse shear waves traveled inside the phantom to drive a longitudinal shear wave [13].

To mimic biological tissues properties, two homogeneous phantoms with 0.5% (w/v) and 0.7% (w/v) agars and one mixed phantom with 0.5% on the top and 0.7% at the bottom were used to validate longitudinal shear wave measurements. Based on coaxial excitation and OCT scanning, the visualization of the longitudinal shear wave is shown in Figure 6. The shear wave in the OCE images can be measured by $\Delta d/\Delta t$ where Δd is travel distance and Δt is time. B-scan OCT images show no obvious difference between the 3 phantoms. However, M-scan Doppler OCT images indicate that the shear velocity is higher in the 0.7% phantom compared to the 0.5% one. The average velocities in the 0.5% and 0.7% phantoms were 1.7 m/s and 3.2 m/s, respectively. In the two-layer phantom sample, one sees an obvious change of shear wave travel speed at the boundary of the layers. The shear wave travel speed was calculated as 1.6 m/s and 3.5 m/s, respectively, in 0.5% and 0.7% phantoms.

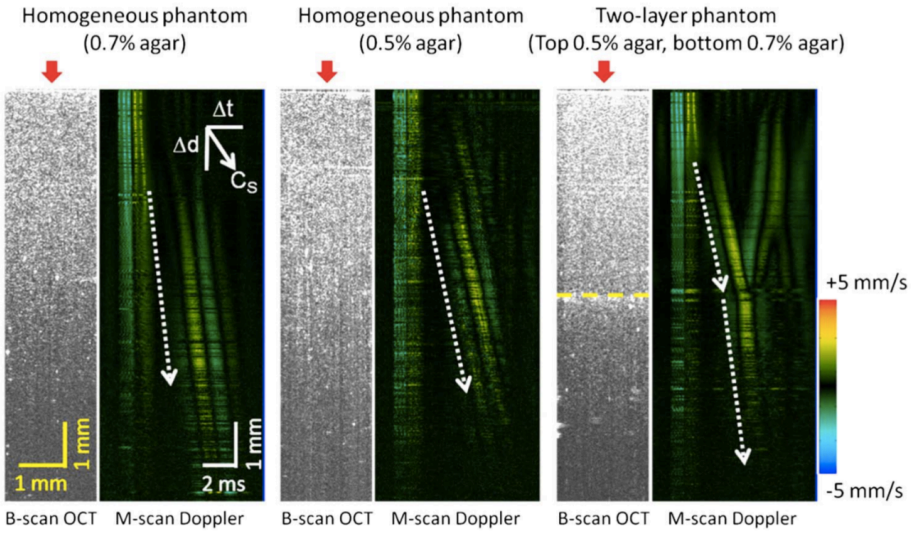

Figure 6. Longitudinal shear wave imaging using coaxial excitation in 0.5%, 0.7% and two-layer phantoms. The shear wave velocity is higher in the 0.7% agar phantom. The shear wave traveling speed obviously changed at the boundary of the layer in the two-layer phantom [13].

Based on the shear wave velocity, Young's modulus E can be calculated as

$$E = 2\times(1+v)\times\rho\times C_s^2$$

where ρ is the density of the sample, v is the Poisson's ratio, and Young's modulus for 0.5% and 0.7% phantoms are 8.7 kPa and 30.7 kPa, respectively, which are very close to the mechanical tests showing Young's modulus for 0.5% and 0.7% phantoms as 9.3 kPa and 29.3 kPa, respectively.

In this study, we developed coaxial longitudinal shear wave measurements with an OCE system that can accurately acquire elastic information along the force direction which is essential for the biomechanical assessment of anisotropic tissues. Also, the orientation of the OCT and PZT units are convenient in many clinical applications since they're located on the same side of the sample.

2.2 Viscosity Monitoring in Blood Coagulation

Blood coagulation analysis is essential in trauma and surgery. Coagulopathic changes in massive bleeding may cause serious problems. Regular coagulation analysis includes measurements of activated partial thromboplastin time (aPTT), prothrombin time (PT), platelet count and fibrinogen levels in plasma [4]. However, all these traditional analyses take more than 30 to 60 minutes. Thromboelastography and thromboelastometry (TEG/ROTEM) can access clot information but have poor sensitivity and repeatability. Therefore, rapid and accurate clot diagnostic systems are needed for assessment of hemodiluted blood coagulation.

In this study, my lab members and I developed a PZT-OCE system that measured the real-time viscous property of one drop of blood. Employed with OCT, the OCE system can detect sample deformation, vibration, or wave propagation which assess tissue biomechanics [13,14]. By measuring the attenuation coefficient of a compressional wave induced by a PZT, viscous properties during the blood coagulation process can be determined. Viscous properties change when the attenuation coefficient of the sample increases. Therefore, dynamic blood coagulation status can be monitored by relating changes of the attenuation coefficient to clinically relevant coagulation metrics, such as coagulation time and clot formation rate [15].

In this study, fresh citrated porcine whole blood (Sierra for Medical Science, CA) was used. The OCE system includes an OCT image unit and a PZT excitation unit. The schematic diagram is shown in Figure 7.

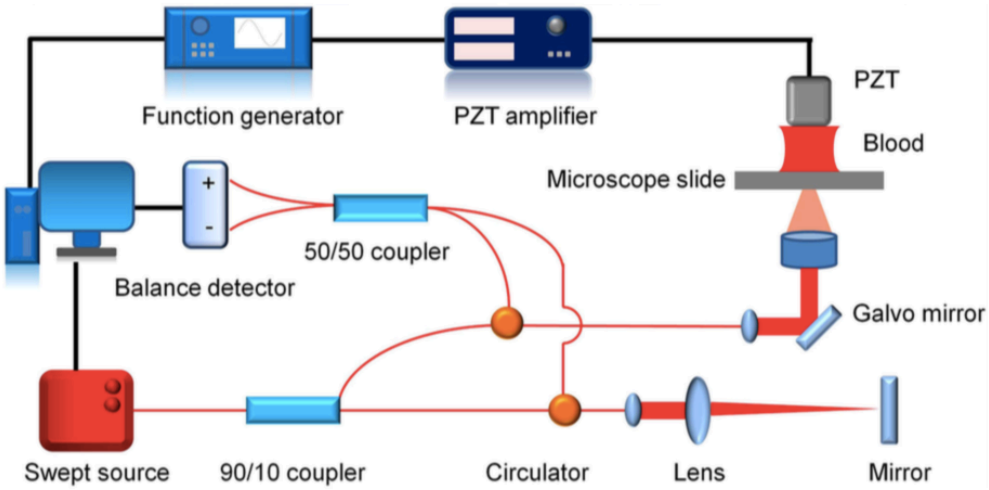

Figure 7. PZT-OCE system for monitoring viscosity during blood coagulation. A drop of blood was placed on a microscope slide. A PZT slightly touches the top of the blood and excited the blood to generate a compressional wave. The vibration is then detected by the Doppler OCT system which is scanning from the bottom of the blood [10].

A drop of porcine blood with a volume of 200 μL was injected onto a microscope slide with a contact area around 141 mm^2. A PZT was attached to the top of the blood drop by surface tension with contact around 64 mm^2. The thickness of the blood drop was 2 mm and stay unchanged during the measurement. The PZT generated one cycle of a sine wave with a frequency of 200 Hz and a peak-to-peak voltage of 70.8 V onto the blood, causing vibration and generation of a compressional wave. The OCT lens was located under the microscope slide. The system used a swept source with a central wavelength of 1310 nm and an A-line speed of 50 kHz. The incoming beam was split by a coupler with 90% of the power going to the sample arm while 10% went to the reference arm. The vibration velocity was detected by Doppler OCT based on phase shift measurement based on the following equation:

$$\mathrm{V} = \frac{\lambda_0 \times \Delta\psi}{4\pi \times n \times \Delta t}$$

where V is the vibration velocity, the phase shift is the vacuum center wavelength (λ_0=1310 nm), n is the refractive index (n=1.4) and Δt is the time interval.

Three test series were made. For the feasibility test, 600 μL of fresh porcine blood was first mixed with buffered $CaCl_2$ (0.2 mol/L, 40 μL) and activator kaolin solution (12.8 g/L, 40 μL); then a drop of 200 μL of blood solution was placed on the microscope slide. For the hemodilution test, in order to quantify the viscosity changes during blood coagulation, the changes in the attenuation coefficient were measured. Different concentrations of activator kaolin solutions (final concentration of 0.75 g/L and 0.38 g/L, a final concentration of 0.01

mol/L and 0.75 g/L) were added to the blood. For the third series, the blood sample was mixed with a final concentration of 0.38 g/L kaolin and a diluted solution of either NaCl (concentration of 0.9%; Sigma-Aldrich, MO) or VetStarch HES (concentration of 6% 130/0.4; Zoetis, NJ). For each series, 3 blood samples of 200 μL were tested for 10 min and the coagulation metrics were measured with the PZT-OCE system.

After excitation from the PZT, a compressional wave was generated and kept attenuated while propagating from the surface of the blood to the bottom. Due to the attenuation, the wave displacement amplitude decreased following the power-law, frequency-dependent attenuation equation:

$$A(\Delta x) = A(0) \times e^{-\alpha \Delta x}$$

where A(0) and A(Δx) are the amplitude of the compressional wave at the initial point and after a travel distance (Δx). The α is the attenuation coefficient of a compressional wave, which is mainly depended on the tissue viscosity with a given wave frequency:

$$\alpha = \frac{\ln[V_{max}(0)] - \ln[V_{max}(\Delta x)]}{\Delta x}$$

where Vmax(0) and $V_{max}(\Delta x)$ are the maximum vibration velocities at the initial point and at a distance of Δx.

The feasibility test result is shown in Figure 8. Vibration velocities were measured at the PZT surface (Vmax(0) = 4.0 mm/s) as well as at the position where 1.4 mm away $V_{max}(1.4\ mm)$ = 0.9 mm/s). Therefore, the attenuation coefficient factor α of the blood was 1.1 Np/mm at 1.4 mm away from the PZT excitation point.

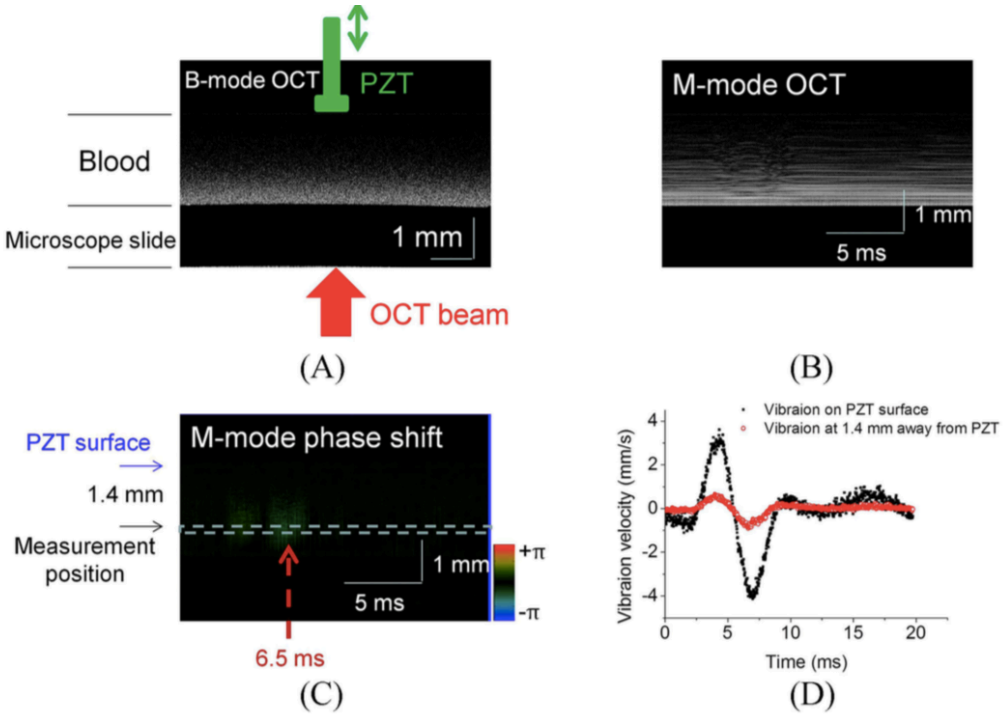

Figure 8. Feasibility test of vibration measurements for blood sample with 0.01 mol/L $CaCl_2$ and 0.75 g/L NaCl. A) OCT images; B) M-scan OCT images; C) Doppler phase images; D) Vibration velocities on the PZT surface and 1.4 mm away from the PZT surface [10].

The attenuation coefficients changed over time during the blood coagulation process. The results for attenuation different concentrations of kaolin are shown in Figure 9.

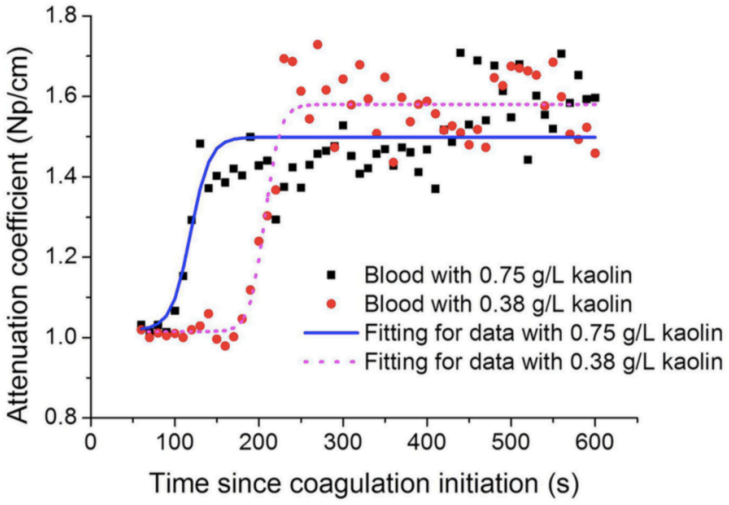

(A)

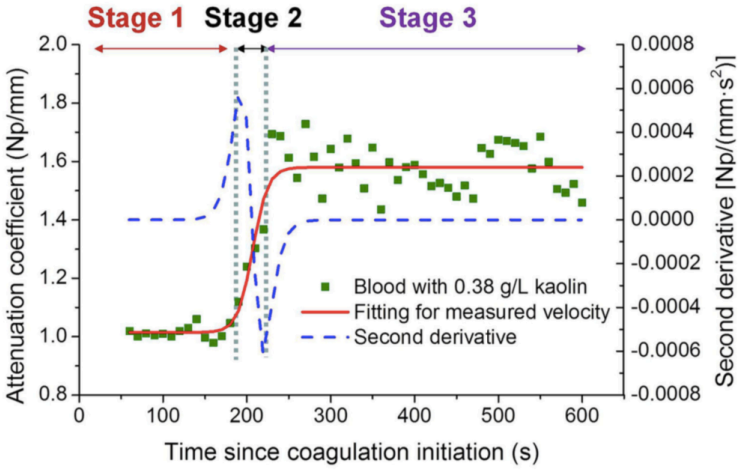

(B)

	Blood with 0.75 g/L kaolin	Blood with 0.38 g/L kaolin
Initial coagulation time [s]	103±6	193±6
Clot formation rate [Np/(mm·s)]	0.0113±0.0019	0.0133±0.0015

(C)

Figure 9. Monitoring blood coagulation with different concentrations of activator kaolin solution. A) Attenuation coefficient plot with 0.75 g/L and 0.38 g/L kaolin solution. B) Changes of the attenuation coefficient in three stages. C) Coagulation metrics [10].

From Figure 9 (A), it is obvious to see a difference in the attenuation coefficient changes between the two different concentrations of kaolin. Figure 9 (B) shows three stages of the changes in the attenuation coefficient. At the first stage, before the blood starts to coagulate, the attenuation coefficient stayed unchanged. Then, it begins to increase rapidly with an increased viscosity at the second stage. The slope of the second stage indicates the clot formation rates. Finally, at the third stage, the attenuation coefficient changes to a small extent and remain stable with the maximum viscosity of the clot. Figure 9 (C) provides the coagulation metric, including the coagulation time and the clot formation rate for blood with 0.75 g/L and 0.38 g/L kaolin solution. The initial coagulation time is longer in blood with a lower concentration of kaolin. However, the clotting rate is similar which corresponds with previous studies [16].

The results of the blood clotting plot with diluted NaCl and HES are shown in Figure 10.

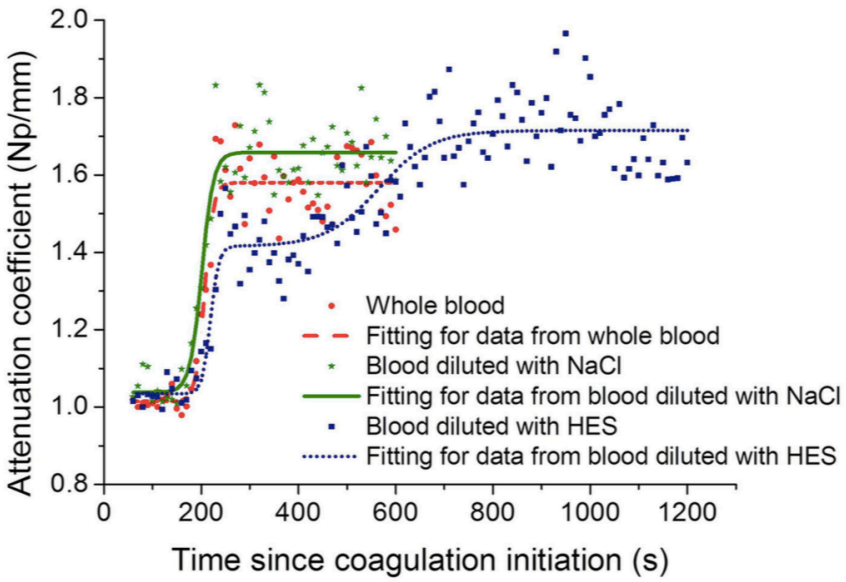

(A)

	Whole blood	Diluted with NaCl	Diluted with HES
Initial coagulation time [s]	193±6	183±15	200±10
Clot formation rate [Np/(mm·s)]	0.0133±0.0015	0.0110±0.0013	0.0015±0.0003

(B)

Figure 10. Monitoring blood coagulation in whole blood and blood with either diluted NaCl or HES. A) Attenuation coefficient plot of the whole blood and blood with diluted NaCl and HES. B) Coagulation metrics [10].

From Figure 10 (A), both whole blood and blood with diluted NaCl showed three stages during the coagulation process. However, 5 stages were observed in the blood sample with HES, including the initial stable state, the rapid transforming stage, the second stable stage, the second transforming stage, and the final stable stage. Clot formation rates were calculated at the first and second stable stages. Three groups had similar initial coagulation time, indicating that the viscosity starts changing almost at the same time. The initial blood clotting process was greatly

affected by hemodilution; yet, it did not significantly change when the blood started to clot and turned into a gel stage when the blood was diluted with NaCl. However, the coagulation formation rate significantly decreased in blood diluted with HES.

In this work, the PZT-OCE system successfully visualized the blood coagulation process in real-time. It can measure the attenuation coefficient directly which closely related to the blood viscosity property. The operation of the measurement is relatively simple by placing a drop of sample blood onto the system. Also, compared to traditional blood coagulation monitoring analysis, the PZT-OCE can rapidly provide information on the clot formation process. Clinically coagulation metrics were quantified to characterize the influence of the activator kaolin and the influence of hemodilution with either NaCl or HES during the coagulation process.

Chapter 3

Development of PS-OCT with Spun Fiber

PS-OCT is a functional extension of traditional OCT. Compared to intensity-based OCT, PS-OCT has the advantage of proving additional contrast information of the sample tissue based on the polarization properties of the light [17, 18].

Several implementation schemes of PS-OCT have been developed so far [6]. In the early days, free-space optics was utilized for controlled polarizations in a PS-OCT system. Polarization maintaining (PM) fibers have been considered for fiber-optic implementation but were found to be less attractive because of increased implementation cost and polarization-mode coupling effects [19]. Lately, PS-OCT systems based on an ordinary single-mode fiber (SMF) have been rigorously researched [18]. In those systems, the polarization state is presumed to be uncontrolled and unknown. Self-calibration techniques are utilized to neutralize the systematic polarization effects based on the Jones matrix or Muller matrix formalism. A complicating factor of the SMF-based PS-OCT systems comes from possible coincidence of the sample-incident polarization state to the sample's characteristic polarization state represented by the principal axis [20]. With uncontrolled polarizations, multiple acquisitions of A-lines or switching the polarization state or simultaneous multiplexed acquisition of multiple polarization inputs become necessary for reliable detection of the polarization states for reflected light signals. Increased system complexity in optical configuration and signal processing reduces the advantage of SMF-based PS-OCT systems [21, 22].

In this work, we present a novel scheme of PS-OCT implementation which takes advantage of a special PM fiber known as a spun fiber (Figure 11). This type of optical fiber has the structure of a PM fiber twisted about the fiber axis. The spun geometry distinguishes two circular polarization (CP) states with different propagation speeds. As ordinary PM fibers have two eigen-modes linearly polarized, the spun fibers have two CP modes with minimal coupling between them. By a nearly symmetric structure, the spun fibers may exhibit reduced sensitivity on fiber bends. Use of the spun fiber in a PS-OCT system is advantageous in terms of orientation insensitivity in fiber connections. In the case of ordinary linear PM fibers, a slight mismatch in angle induces annoying inter-mode coupling. The feature of orientation insensitivity can allow use of a fiber rotary joint which is very important in endoscopic PS-OCT systems.

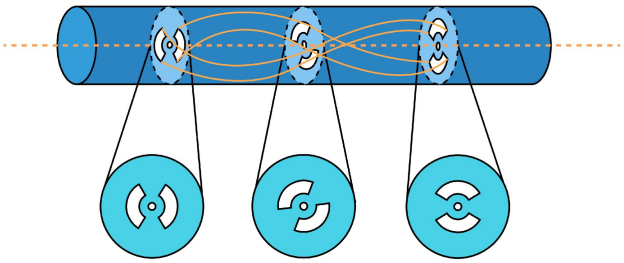

Figure 11: Spun optic fiber. Bow-tie rotates along the optic axis, distinguishing two circular polarization states.

Figure 12 shows the schematic diagram of our PS-OCT system. The VCSEL swept source (SS) with a 1310 nm center wavelength was used as the light source. The main body of the SS-OCT interferometer was constructed with SMF optics for simplicity while the spun fiber was used in the sample arm. Light comes from the laser and was filtered with a linear

polarizer and separated by a 75/25 coupler where 75% of the light went to the sample arm. At the sample arm, the light was tapped out and examined in a polarization state by the SOP monitor. With a polarization-sensitive photodetector, the state was adjusted to be linearly polarized by using a polarization controller placed at the SMF part. Light was launched to the spun fiber in a CP mode after a quarter waveplate (QWP). Thus, the sample-incident light was aligned to be of the CP state as well. The light reflected from the sample was delivered to two balanced photodetectors which detected the respective CP states of the spun fiber. Through careful alignments of polarization controllers with polarization-sensitive detectors, the polarization states were properly controlled in our system and kept unchanged during operation. Meanwhile, the spun fiber exposed to possible physical variations could maintain the CP states in the signal interconnection. Thus, the system was constructed by fiber optics but managed controlled polarization, which largely differs from the operation principle of SMF-based PS-OCT systems developed previously.

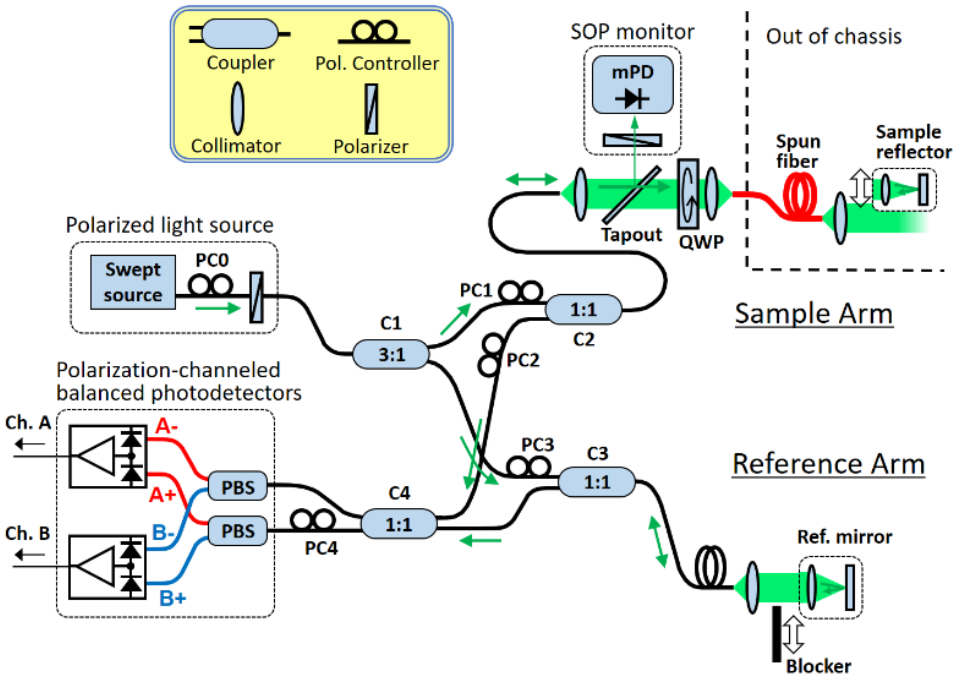

Figure 12: Schematic of the PS-OCT system. PC: polarization controller, C1: 75/25 coupler, C2, C3. C4: 50/50 coupler, QWP: quarter-wave plate, PBS: polarization beam splicer.

We tested our PS-OCT system on a chicken breast sample. Figure 13 shows the results of the proposed system. Due to the birefringent properties of the chicken breast, muscle structures show different sensitivities to the two polarization states. The bright area shown in channel A (horizontal polarization states) becomes dark in channel B (vertical polarization state). Compared with intensity-based images, phase retardation shows clear muscle structures, indicating our PS-OCT system is able to get more information due to its additional contrast.

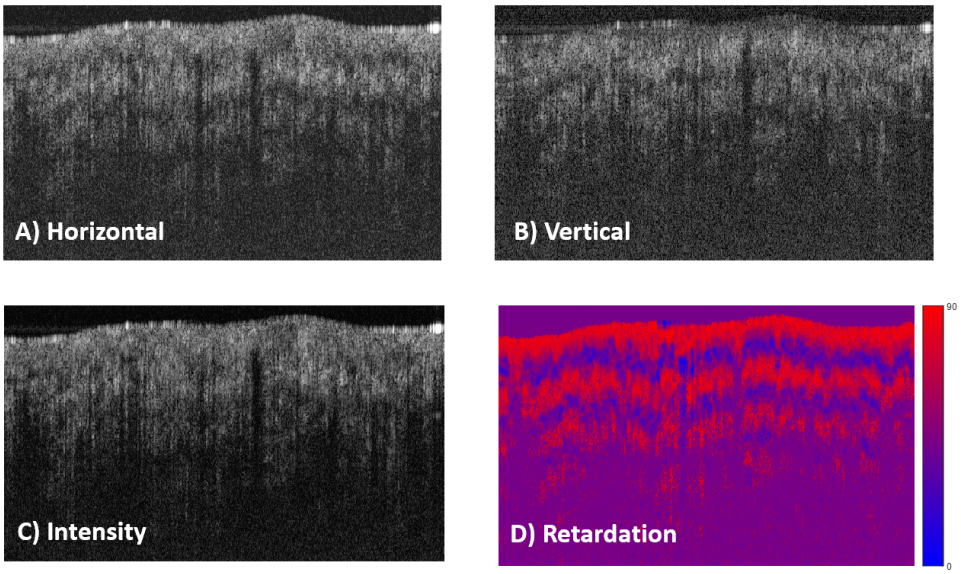

Figure 13: Chicken breast images from upper A) horizontal polarization states, B) vertical polarization states, C) intensity-based image, and lower D) phase retardation image.

Chapter 4

Summary

From this study, we can conclude that OCT is an effective tool to resolve hair follicle density and hair follicle diameter, therefore, making it possible to diagnose androgenic alopecia at an early stage. Since the penetration depth of the OCT beam is approximately 1-2 mm, we'd like to use the 1700 nm center wavelength source for a deeper observation in the future. Also, more patients will be involved for better understanding of androgenic alopecia.

The PZT-OCE system could be used to rapidly and conveniently provide information about the clot formation process in whole blood. Clinical coagulation metrics can also be monitored to characterize the influence of different amount of activator kaolin and the influence of hemodlution with either NaCl or HES on blood coagulation process. There, our PZT-OCE system is powerful in real-time viscosity monitoring assessment during the blood coagulation process. In addition, the PZT-OCE system has the capability to image elasticity of anisotropic biological tissue by measuring the coaxial longitudinal shear wave.

PS-OCT with spun fiber successfully distinguished the two polarization states of a chicken breast sample, which shows great potential in the development of an endoscopic PS-OCT system for additional information on many applications. As future plan, we would like to further research on the spun fiber and try to find out the best condition for the making circular polarization. We also want to apply the PS-OCT system into the study of androgenic alopecia to observe the birefringence of hair follicle.

References

[1] Drexler W, Fujimoto JG. Optical coherence tomography: Technology and applications. Berlin, Heidelberg, New York: Springer-Verlag; 2008.

[2] Wang S, Larin KV. Optical coherence elastography for tissue characterization: a review. J Biophotonics. 2015;8:279-302.

[3] Zhu J, Qu Y, Ma T, Li R, Du Y, Huang S, et al. Imaging and characterizing shear wave and shear modulus under orthogonal acoustic radiation force excitation using OCT Doppler variance method. Opt Lett. 2015;40:2099-102.

[4] Park BH, Saxer C, Srinivas SM, Nelson JS, de Boer JF. In vivo burn depth determination by high-speed fiber-based polarization sensitive optical coherence tomography. Journal of Biomedical Optics. 2001;6:474-9.

[5] Kulkarni MD, Izatt JA, Kobayashi K, Yazdanfar S, Wong RCK, Sivak MV, et al. Optical coherence tomography: a novel tool for micron-resolution biomedical diagnostics. 1997; 2: 883-6.

[6] Roth JE, Kozak JA, Yazdanfar S, Rollins AM, Izatt JA. Simplified technique for polarization-sensitive optical coherence tomography. Opt. Lett. 2001;26:1069-1071.

[7] Barton JK, Welch AJ, Izatt JA. Investigating pulsed dye laser-blood vessel interaction with color Doppler optical coherence tomography. Optics Express. 1998;3.

[8] Wang XJ, Milner TE, Dhond RP, Sorin WV, Newton SA, Nelson TS. Characterization of human scalp hairs by optical low-coherence reflectometry. Optics Letters. 1995;20:524-6.

[9] Q Fang, Andrea Curatolo, Philip Wijesinghe, Yen Ling Yeow, Juliana Hamzah, Peter B. Noble, Karol Karnowski, David D. Sampson, Ruth Ganss, Jun Ki Kim, Woei M. Lee, and Brendan F. Kennedy, "Ultrahigh-resolution optical coherence elastography through a micro-endoscope: towards in vivo imaging of cellular-scale mechanics," Biomed. Opt. Express. 2017;8:5127-5138.

[10] X. Xu, J. Zhu, J. Yu and Z. Chen, "Viscosity Monitoring During Hemodiluted Blood Coagulation Using Optical Coherence Elastography," *IEEE Journal of Selected Topics in Quantum Electronics*. 2019;25:1-6.

[11] Jiang Zhu, Xingdao He, and Zhongping Chen, "Perspective: Current challenges and solutions of Doppler optical coherence tomography and angiography for neuroimaging", APL Photonics. 2018;3:12.

[12] Qu Y, Ma T, He Y, Yu M, Zhu J, Miao Y, et al. Miniature probe for mapping mechanical properties of vascular lesions using acoustic radiation force optical coherence elastography. Sci Rep. 2017;7:4731.

[13] Jiang Zhu, Junxiao Yu, Yueqiao Qu, Youmin He, Yan Li, Qiang Yang, Tiancheng Huo, Xingdao He, and Zhongping Chen, "Coaxial excitation longitudinal shear wave measurement for quantitative elasticity assessment using phase-resolved optical coherence elastography," Opt. Lett. 2018; 43:2388-2391.

[14] Jiang Zhu, Yueqiao Qu, Teng Ma, Rui Li, Yongzhao Du, Shenghai Huang, K. Kirk Shung, Qifa Zhou, and Zhongping Chen, "Imaging and characterizing shear wave and shear modulus under orthogonal acoustic radiation force excitation using OCT Doppler variance method," Opt. Lett. 2015;40:2099-2102.

[15] Brezinski ME, Tearney GJ, Bouma BE, Izatt JA, Hee MR, Swanson EA, et al. Optical coherence tomography for optical biopsy. Properties and demonstration of vascular pathology. Circulation. 1996;93:1206-13.

[16] X. Xu, J. Zhu, and Z. Chen, "Dynamic and quantitative assessment of blood coagulation using optical coherence elastography," *Sci. Rep*. 2016;6:24294.

[17] de Boer JF, Milner TE, van Gemert MJC, Nelson JS. Two-dimensional birefringence imaging in biological tissue using polarization-sensitive optical coherence tomography. Opt Lett. 1997;22:934-36.

[18] Sucei Moon, Yusi Miao, Zhongping Chen, "Fiber-based polarization optical coherence tomography of a minimalistic system cofiguration", Otp Lett. 2019;

[19] S. Rivet, M. J. Marques, A. Bradu, A. Podoleanu, M. R. Hee, E. A. Swanson, J. G. Fujimoto, and D. Huang, "Passive optical module for polarization-sensitive optical coherence tomography systems References and links," Opt. Express. 2017;25:15533-14544.

[20] J. Zhang, W. Jung, J. S. Nelson, and Z. Chen, "Full range polarization-sensitive Fourier domain optical coherence tomography," Opt. Express. 2004;12:6033.

[21] S. Moon and Z. Chen, "Phase-stability optimization of swept-source optical coherence tomography.," Biomed. Opt. Express. 2018;9:5280–5295.

[22] S. Moon, Y. Qu, and Z. Chen, "Characterization of spectral-domain OCT with autocorrelation interference response for axial resolution performance," Opt. Express. 2018; 26:7253.

Appendix

A. E. Heidari, **Junxiao Yu** *et al*., "Optical Coherence Tomography as an Oral Cancer Screening Adjunct in a Low Resource Settings," in *IEEE Journal of Selected Topics in Quantum Electronics*, vol. 25, no. 1, pp. 1-8, Jan.-Feb. 2019, Art no. 7202008. (2018)

Jiang Zhu, **Junxiao Yu**, Yueqiao Qu, Youmin He, Yan Li, Qiang Yang, Tiancheng Huo, Xingdao He, and Zhongping Chen, "Coaxial excitation longitudinal shear wave measurement for quantitative elasticity assessment using phase-resolved optical coherence elastography," Opt. Lett. 43, 2388-2391 (2018)

X. Xu, J. Zhu, **J. Yu** and Z. Chen, "Viscosity Monitoring During Hemodiluted Blood Coagulation Using Optical Coherence Elastography," in *IEEE Journal of Selected Topics in Quantum Electronics*, vol. 25, no. 1, pp. 1-6, Jan.-Feb. 2019, Art no. 7200406. (2018)

Yan Li, Joseph Jing, **Junxiao Yu**, Buyun Zhang, Tiancheng Huo, Qiang Yang, and Zhongping Chen, "Multimodality endoscopic optical coherence tomography and fluorescence imaging technology for visualization of layered architecture and subsurface microvasculature," Opt. Lett. 43, 2074-2077 (2018)